# SONOWORLD: TOWARDS INTERACTIVE POSE-CONTROLLABLE ULTRASOUND WORLD MODELS

**Anonymous authors**
Paper under double-blind review

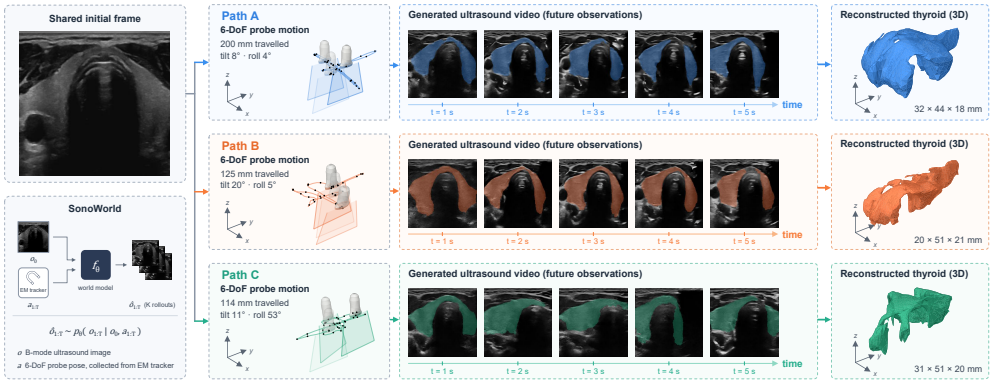


Figure 1: Starting from the same initial ultrasound frame, SonoWorld generates distinct sequences of future ultrasound views along different 6-DoF probe scan paths, which captures how probe motion determines the evolving image appearance and ultimately the reconstructed 3D thyroid anatomy.

## ABSTRACT

Robotic ultrasound can standardize image acquisition and reduce operator workload and variability, but policy learning remains limited by the lack of realistic, controllable simulation environments: physical phantoms and acoustic simulators exhibit a substantial domain gap from clinical images, and trial-and-error exploration on patients is unsafe. While controllable world models have advanced rapidly in natural-image domains, ultrasound world modeling remains challenging because each frame captures only a cross-section of unobserved 3D anatomy, causing small probe motions to induce large appearance changes. Existing approaches rely on robot-tracked poses and latent-space prediction, but do not directly generate the observations required for interactive control. We propose SonoWorld, a causal ultrasound world model that learns video dynamics from unlabeled clinical videos and grounds them to 6-DoF control using a small set of freehand clinical scans tracked with an electromagnetic (EM) sensor. SonoWorld is trained in three stages: pretraining a latent-action-conditioned video diffusion model on around 6.9 million unlabeled multi-organ ultrasound frames; grounding the learned video dynamics to metric probe poses with a small EM-tracked thyroid dataset; and applying distribution matching distillation to enable causal, long-horizon autoregressive generation with selectively caching eviction tokens at inference time. We evaluate controllability through pose-following fidelity, round-trip consistency, and axis-specific control under synthetic actions on held-out tracked scans, and further validate it with a user study. In model-based action discrimination, SonoWorld correctly ranks the target-directed probe motion over an equal-magnitude opposite motion in up to 74.8% of trials. To our knowledge, SonoWorld is the first causal, pose-controllable ultrasound world model learned primarily from freehand clinical videos, providing a data-driven interactive environment for robotic ultrasound data acquisition and policy evaluation. Project page is available under `https://iclr2027anonymous.github.io/SonoWorld/`.

## 1 INTRODUCTION

Ultrasound is among the most widely used diagnostic imaging modalities, valued for its real-time imaging, absence of ionizing radiation, portability, and low cost (Wang et al., 2020; Jiang et al.,



Reviewers: please read the Reviewer Guidelines (iclr.cc/Conferences/2027/ReviewerGuidelines) and the AI Policy for Reviewers (iclr.cc/Conferences/2027/AIPolicyForReviewers). If you used AI to expand, edit, or polish your review, please provide the input text to the LLM. Better still, consider skipping the LLM and submitting your original text: we, and the authors, are much more interested in your unedited thoughts than in what an LLM has to say. AI-assisted or not, you are putting your name and reputation behind your review: LLM-generated falsehoods, hallucinations or misrepresentations are subject to disciplinary action, which may include desk-rejecting all papers you have authored.

2023). Unlike many imaging modalities, however, ultrasound acquisition is inherently interactive: the observed image depends on the six-degree-of-freedom (6-DoF) pose of a hand-held probe, which the operator continuously adjusts to navigate anatomy and acquire diagnostically standard views. Consequently, image quality and diagnostic yield depend heavily on operator expertise, contributing to substantial inter-operator variability and a persistent shortage of trained sonographers (Jiang et al., 2023). Robotic ultrasound offers a promising path toward standardized image acquisition, reduced operator workload, and broader access to expert-level scanning, particularly in remote and resource-limited settings (Du et al., 2024). Realizing this potential requires robotic scanning policies that map observed ultrasound images to probe motions, whose development and evaluation in turn require realistic interactive environments in which the visual consequences of probe actions can be observed.

Existing environments for robotic ultrasound expose a fundamental trade-off between controllability, realism, and safety. Physical phantoms and physics-based simulators permit controlled exploration over probe poses, but their synthetic anatomy and image formation leave a substantial domain gap from clinical ultrasound (Shams et al., 2008; Bürger et al., 2013; Gao et al., 2009). Re-slicing reconstructed 3D ultrasound volumes provides more realistic observations, but requires subject-specific tracked acquisitions and cannot faithfully reproduce view-dependent appearance changes under arbitrary probe orientations (Lasso et al., 2014). Scanning real patients provides observations from the true clinical distribution, yet repeated trial-and-error exploration is neither practical nor safe. An alternative line of work bypasses explicit simulation and learns probe guidance or autonomous scanning directly from tracked clinical scans and expert demonstrations (Jiang et al., 2024b;a; Yue et al., 2025; Su et al., 2024; Jiang et al., 2025). While effective, this paradigm depends on collecting real image–action trajectories at scale and does not provide a reusable environment for evaluating counterfactual probe actions before they are executed on patients. These limitations motivate a controllable generative environment learned directly from clinical ultrasound videos, capable of synthesizing realistic future observations in response to probe actions without tracking each patient.

Controllable world models offer a promising data-driven alternative by learning to predict future observations conditioned on actions, and have emerged as powerful interactive simulators for games, autonomous driving, and robotic manipulation (Hou et al., 2026; Ding et al., 2025; Gao et al., 2026a). Ultrasound, however, presents a distinct challenge: each frame captures only a 2D cross-section of unobserved 3D anatomy, such that small probe motions, particularly out-of-plane translations and rotations, can induce large changes in image appearance. Existing ultrasound world models address this challenge using robot-tracked acquisitions (Fan et al., 2026) and latent-space prediction (Yue et al., 2025; Jiang et al., 2024b), but do not directly generate future ultrasound observations from freehand 6-DoF probe actions. Consequently, a causal, pose-controllable world model that can generate realistic ultrasound observations directly from clinical data remains largely unexplored.

We introduce SonoWorld, a causal, pose-controllable ultrasound world model that learns ultrasound video dynamics primarily from large-scale unlabeled clinical videos and requires only a small set of EM-tracked scans to acquire 6-DoF control. Inspired by previous works (Gao et al., 2025; 2026a), SonoWorld is trained in three stages: First, we pretrain a latent-action video diffusion model on around 6.9 million unlabeled multi-organ ultrasound frames, allowing it to capture both probe-induced appearance changes and physiological dynamics without pose annotations. Second, we ground the learned dynamics to physical probe motion by post-training on a small set of calibrated EM-tracked thyroid scans, where probe motion is represented as relative 6-DoF actions in the probe coordinate frame. Finally, we distill the bidirectional model into a causal autoregressive generator using self-forcing and selectively retain informative KV-cache tokens, enabling stable long-horizon interactive rollouts. Our main contributions are summarized as follows:

- We introduce **SonoWorld**, to our knowledge the first causal, interactive, pose-controllable ultrasound world model that directly generates future ultrasound observations conditioned on 6-DoF probe actions, providing an interactive learned environment for robotic ultrasound data acquisition and policy evaluation.
- We develop a scalable training strategy that learns ultrasound dynamics from around 6.9 million unlabeled multi-organ clinical frames and grounds them to probe control using only a small set of EM-tracked scans. This enables large-scale dynamics learning without pose annotations, while requiring costly tracker-acquired data only for the subsequent physical action-grounding stage.
- We convert the bidirectional video model into a causal autoregressive generator through self-forcing and introduce selective KV-cache retention for streaming inference, enabling extended action-conditioned rollouts while preserving generation quality.

- We evaluate SonoWorld under measured, accelerated, round-trip, and axis-specific synthetic probe motions, and further conduct a user study with experienced ultrasound raters assessing image quality, video consistency, and probe–anatomy alignment.

## 2 Related Work

**Generative World Models** Generative world models learn action-conditioned dynamics of visual environments and have emerged as a scalable paradigm for interactive simulation across embodied AI (NVIDIA et al., 2025; Yang et al., 2024; Jang et al., 2025; Gao et al., 2026a; Huang et al., 2026a), games (Bruce et al., 2024; Alonso et al., 2024; Kanervisto et al., 2025), autonomous driving (Hu et al., 2023; Gao et al., 2024b; Yang et al., 2025). A central challenge in scaling such models is that action-labeled data are far less abundant than passive video. Latent-action models address this imbalance by discovering control-relevant dynamics directly from visual observations: Genie (Bruce et al., 2024) learns discrete latent actions, AdaWorld (Gao et al., 2025) extends them to a continuous action space, and subsequent work like DreamDojo scales this paradigm to real-world robotic application (Gao et al., 2026a) and grounds learned latent actions into executable robot commands (Ye et al., 2025). This separation between learning visual dynamics from abundant unlabeled video and grounding them to physical actions provides a natural foundation for domains where paired action–video data are costly to acquire.

**Medical World Models** In the medical field generative world models have recently emerged as learned simulators for medical video. Endora (Li et al., 2024) models spatiotemporal dynamics to generate realistic endoscopic videos, while Surgical Vision World Model (Koju et al., 2025) learns latent actions from unlabeled surgical videos for controllable generation, and SAW (Rapuri et al., 2026) further conditions laparoscopic video generation on language, tissue affordances, and 2D tool trajectories. In ultrasound, Cardiac Copilot (Jiang et al., 2024b) learns a latent spatial model from tracked echocardiography and predicts structural features of neighboring cardiac planes for probe guidance; Structure-aware World Model (Jiang et al., 2024a) extends this paradigm with large-scale self-supervised learning of anatomical representations under 3D pose transformations; and EchoWorld (Yue et al., 2025) incorporates motion-induced visual dynamics and visual–motion history for sequential probe guidance, but these methods use world modeling primarily for representation learning rather than as image-generating interactive environments. More recently, Fan et al. (Fan et al., 2026) predict future ultrasound observations conditioned on tracked probe motions and use the learned dynamics for goal-plane navigation. In contrast, SonoWorld learns ultrasound dynamics primarily from large-scale untracked clinical videos, grounds them to metric 6-DoF probe actions using a small tracked subset, and causally generates future observations under these actions, enabling interactive rollouts for policy evaluation and model-based action discrimination.

**Interactive Ultrasound Environments** Several strategies exist for building an environment in which probe motion can be explored. Physical phantoms provide genuine acoustic interaction but lack clinical appearance and encode a single fixed anatomy. Physics-based simulation renders images from a CT-derived anatomical model at arbitrary poses (Shams et al., 2008; Bürger et al., 2013; Salehi et al., 2015), yet ray-casting cannot reproduce speckle from first principles (Gao et al., 2009) and wave-accurate solvers are too slow to be interactive (Jaros et al., 2016). General-purpose robotics platforms such as NVIDIA Isaac Sim support scalable robotic ultrasound simulation and policy training, but their simplified ultrasound image formation does not faithfully capture the acoustic properties of clinical ultrasound (Gao et al., 2026b). Sim-to-real translation narrows the appearance gap (Vitale et al., 2020) at the cost of physical consistency. Freehand reconstruction compounds a tracked sweep into a volume that can be re-sliced (Lasso et al., 2014), but view-dependent effects are frozen at the acquisition angle and every simulated subject needs its own tracked acquisition. Scanning real patients is the fidelity upper bound (Su et al., 2024; Jiang et al., 2025), yet a scan traverses a single trajectory and cannot report what a different motion would have produced. A learned world model addresses these limitations, inheriting real appearance, view-dependent acoustics and physiological motion from clinical video, covering anatomical variation across patients, and answering potential pose queries without per-subject tracking.

## 3 Methods

### 3.1 Foundational Ultrasound Video Diffusion Model

**Ultrasound video dynamics encoding.** Ultrasound video dynamics arise from both probe motion, which changes the imaged anatomical cross-section, and physiological motion, such as cardiac con-

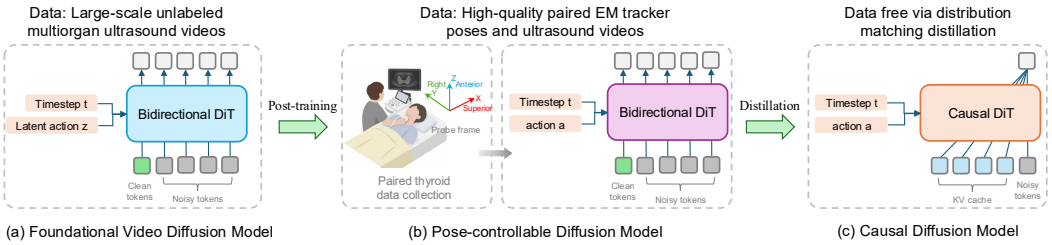


Figure 2: Three stages of ultrasound world model development. (a) **Pretraining.** A bidirectional DiT is trained on large-scale unlabeled multi-organ ultrasound videos, conditioned on the diffusion timestep $t$ and latent actions $\mathbf{z}$ via adaptive layer normalization. (b) **Post-training.** The model is then post-trained on high-quality thyroid ultrasound videos paired with EM tracker poses, replacing the latent action with the physical action. (c) **Causal transform.** The bidirectional model is finally distilled into a causal DiT via distribution matching distillation (DMD) Yin et al. (2024).

traction, respiration, and vascular pulsation. To capture these dynamics without action annotations, we learn a latent action model (LAM) inspired by AdaWorld (Gao et al., 2025). Given a clip $\mathbf{x}^{1:K}$, the encoder patchifies each adjacent frame pair $(\mathbf{x}^i, \mathbf{x}^{i+1})$ into $16 \times 16$ patches, appends a learnable action token to each frame, and processes them with alternating spatial and temporal attention. The action token of $\mathbf{x}^{i+1}$ is compressed into a 32-dimensional latent action $\mathbf{z}^i$, while the patch tokens are discarded. A decoder reconstructs $\mathbf{x}^{i+1}$ from $\mathbf{x}^i$ and $\mathbf{z}^i$. This low-dimensional bottleneck encourages $\mathbf{z}^i$ to encode frame-to-frame dynamics rather than appearance shared across frames. Full architectural details are provided in Appendix Fig 5.

**Conditional video diffusion model training.** We next train an action-conditioned image-to-world model that predicts future observations from an initial frame and a sequence of latent actions. We build on Wan2.1-T2V-1.3B (Wan et al., 2025), a latent video diffusion transformer, and encode each clip $\mathbf{x}^{1:K}$ into $\mathbf{y} = \mathcal{E}(\mathbf{x}^{1:K})$ using the pretrained Wan VAE $\mathcal{E}$. Generation is conditioned on the initial frame $\mathbf{x}^1$ and latent actions $\mathbf{z}^{1:K-1}$. We inject each $\mathbf{z}^i$ through adaptive layer normalization (AdaLN) (Xu et al., 2019) by projecting it to the model dimension, adding it to the diffusion timestep embedding, and mapping the result to per-block modulation parameters. The action projection is zero-initialized to preserve the pretrained video prior at the start of training. We optimize the model with flow matching (Lipman et al., 2023; Liu et al., 2023). Given Gaussian noise $\boldsymbol{\epsilon}$ and $t \sim \mathcal{U}[0, 1]$, we define $\mathbf{y}_t = (1-t)\mathbf{y} + t\boldsymbol{\epsilon}$ and train the velocity predictor $\mathbf{u}_\theta$ as

$$\mathcal{L}_{\text{flow}}(\theta) = \mathbb{E}_{\mathbf{y},\boldsymbol{\epsilon},\mathbf{c},t}\left[\left\|\mathbf{u}_\theta(\mathbf{y}_t, t, \mathbf{c}) - (\boldsymbol{\epsilon} - \mathbf{y})\right\|_2^2\right], \tag{1}$$

where $\mathbf{c} = (\mathbf{x}^1, \mathbf{z}^{1:K-1})$ denotes the initial-frame and latent-action conditions. Video diffusion model training is detailed in Appendix A.4.

### 3.2 Pose-Controllable Video Diffusion Model

The latent actions learned during pretraining capture transition dynamics but lack physical units and therefore cannot directly control probe motion. We acquire freehand clinical scans with an EM tracker and calibrate the tracked sensor poses to the probe tip. We then express consecutive poses as relative 6-DoF motions in the probe frame (Fig. 3) and replace the latent actions with these metric actions to post-train the pretrained model on the EM-tracked subset.

**Pose calibration.** The tracked sensor sits on the probe handle. The imaging plane is attached to the tip, so a constant rigid offset, the lever arm, must be composed onto every sample (Fig. 3(a)(b)). Each scan records two synchronized streams: a sensor clamped to the probe and a second sensor taped to the patient, which measures patient motion. Each stream provides, at every sample $t$, a unit quaternion $\mathbf{q}_t$, a position $\mathbf{p}_t \in \mathbb{R}^3$ in millimetres, and a tracking quality $\kappa_t$, from which we form the homogeneous transform $\mathbf{T}_{\text{world}\leftarrow\text{sensor}}(t) = [\mathbf{R}(\mathbf{q}_t) \mid \mathbf{p}_t] \in SE(3)$, where $\mathbf{T}_{B\leftarrow A}$ denotes the transform taking coordinates in frame $A$ to frame $B$. The lever arm is obtained from the manufacturer-supplied probe-to-sensor matrix by two signed axis relabellings, yielding the constant transform $\mathbf{T}_{\text{sensor}\leftarrow\text{tip}} = [\mathbf{R}_{\text{st}} \mid \mathbf{r}]$, whose translation $\mathbf{r}$ is the tip position in sensor coordinates ($\|\mathbf{r}\| \approx 119.2$ mm for the thyroid probe). Let $\mathbf{T}^{\text{probe}}_{\text{world}\leftarrow\text{sensor}}(t)$ and $\mathbf{T}^{\text{ref}}_{\text{world}\leftarrow\text{sensor}}(t)$ denote the probe-

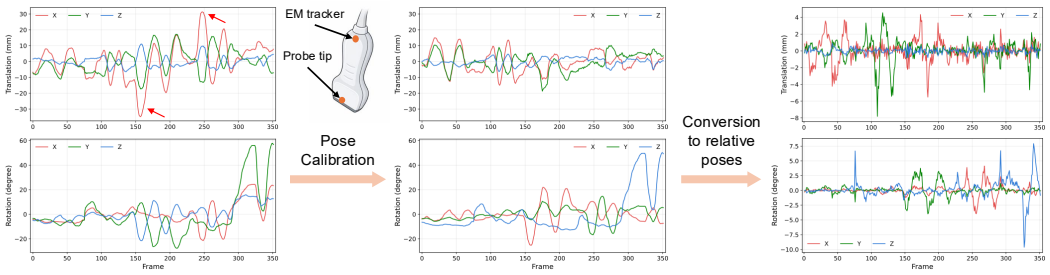


(a) EM tracker poses in world frame (b) Probe-tip poses in world frame (c) Probe-tip poses in probe frame

Figure 3: EM-tracked pose preprocessing pipeline (a) Raw EM sensor poses are expressed in world frame and are affected by the lever arm between the sensor and probe tip. (b) A fixed sensor-to-tip calibration transforms the measurements to probe-tip poses, such that the resulting motion corresponds to that of the imaging plane. (c) Consecutive probe-tip poses are converted to relative motions expressed in the preceding probe frame, yielding 6-DoF actions used to condition SonoWorld.

and patient-sensor streams. The probe-tip pose in the patient frame factorizes as

$$\mathbf{T}_{\text{patient}\leftarrow\text{tip}}(t) = \left(\mathbf{T}^{\text{ref}}_{\text{world}\leftarrow\text{sensor}}(t)\right)^{-1} \mathbf{T}^{\text{probe}}_{\text{world}\leftarrow\text{sensor}}(t)\, \mathbf{T}_{\text{sensor}\leftarrow\text{tip}}. \tag{2}$$

Eq. equation 2 successively maps tip coordinates into the probe-sensor, world, and patient frames. Derivation of pose calibration is detailed in Appendix A.2.

**Conversion to relative poses.** The action must describe the operator's motion rather than the orientation and placement of the patient, so absolute world poses are unusable as conditioning. The pose stream is therefore converted to relative poses expressed in the probe's own frame. Abbreviating $\mathbf{T}(t) \equiv \mathbf{T}_{\text{patient}\leftarrow\text{tip}}(t)$, the relative pose between any ordered pair of samples $(s, t)$ is

$$\mathbf{T}_{s\to t} = \mathbf{T}(s)^{-1}\,\mathbf{T}(t) = \begin{bmatrix} \mathbf{R}_s^\top \mathbf{R}_t & \mathbf{R}_s^\top(\mathbf{p}_t - \mathbf{p}_s) \\ \mathbf{0}^\top & 1 \end{bmatrix}, \tag{3}$$

where $\mathbf{R}_t$ and $\mathbf{p}_t$ are the rotation and translation blocks of $\mathbf{T}(t)$, and $\mathbf{T}_{s\to t}$ denotes the motion of the probe frame from sample $s$ to sample $t$ (Fig. 3(c)). The patient frame cancels between the two factors, so left-multiplying the whole stream by any fixed transform leaves Equation. 3 unchanged, and the translation is resolved in the local axes of the start sample: advancing a fixed distance along the beam is the same action wherever on the body it occurs. Since $SE(3)$ is not a vector space, we map the relative pose to $\mathbb{R}^6$ by concatenating its translation with the $\mathfrak{so}(3)$ logarithm of its rotation,

$$\mathbf{a}_{s\to t} = \left[\, \mathbf{R}_s^\top(\mathbf{p}_t - \mathbf{p}_s) \;\|\; \log\!\left(\mathbf{R}_s^\top \mathbf{R}_t\right)^\vee \right] \in \mathbb{R}^6, \tag{4}$$

with translation in millimetres and rotation in radians.

**Post-training with EM-tracked actions.** We introduce a *chunk action*, in which every frame carries its cumulative motion since the start of its own four-frame window, matching the temporal compression of the Wan VAE. Within each four-frame window, each frame is represented by its cumulative motion from the window start, and the four 6-DoF motions are concatenated into a 24-dimensional action. Post-training is initialized from the pretrained model with the latent-action pathway replaced by a new metric-action pathway. Each chunk action is projected from $\mathbb{R}^{24}$ to the model dimension and added to the corresponding timestep embedding before adaptive layer normalization, with a zero action assigned to the initial latent frame. Generation is conditioned on the first clean latent frame, encoded as a prefix by concatenating the masked clean latents with a binary mask indicating observed frames and projecting them through a parallel convolution added to the backbone patch embedding. Both the action projection and prefix convolution are zero-initialized, preserving the pretrained function at initialization. The entire DiT generator is then trained end-to-end with all parameters unfrozen.

### 3.3 Causal Video Diffusion Model

The post-trained model uses bidirectional attention over all latent frames and therefore denoises an entire clip jointly, precluding interactive generation. An interactive probe simulator requires that the next block of frames be emitted as soon as the operator supplies the next action. We therefore convert the model into an efficient block-causal, few-step generator that attends only backward in

time and carries a KV cache across blocks. Direct autoregressive training, however, introduces exposure bias (Bengio et al., 2015; Chen et al., 2024; Liu et al., 2026): a model trained on ground-truth context must condition on its own predictions at inference, causing errors to accumulate over long rollouts. We therefore adopt self-forcing distillation (Huang et al., 2026b), in which each block is generated from a KV cache constructed from the student's own preceding outputs, reducing the mismatch between training and autoregressive inference. Long-horizon generation additionally requires controlling the growth of the KV cache. Existing streaming video generators bound memory by retaining an attention sink and a recent temporal window while discarding intermediate history (Liu et al., 2026; Lu et al., 2026). We instead treat the choice of which frames to retain as a selection problem. Inspired by heavy-hitter eviction in language models (Zhang et al., 2023), we score each cached frame by the attention mass it has received and retain the highest-scoring frames alongside the sink and the recent window, applying rotary embeddings when keys are written into the cache so that retained frames keep their original positions. At inference, SonoWorld can generate ultrasound video at 40.6 fps at $256 \times 256$ resolution using four denoising steps on a single NVIDIA H100, enabling interactive action-conditioned rollouts.

# 4 Experiments

## 4.1 Datasets

**Unlabeled ultrasound videos.** Under IRB approval, we collect a large-scale corpus of freehand ultrasound videos acquired during routine clinical examinations, without any probe-pose annotation. The raw corpus consists of 64,599 video files spanning three anatomical regions: abdomen (31,209 files, 48.3%), thyroid (21,399 files, 33.1%), and cardiac (11,991 files, 18.6%), totaling 15,357,337 frames. Because clinical recordings are noisy, we design an automated filtering pipeline that removes colour Doppler acquisitions, discards static segments, and excludes segments without probe–skin contact. Retained segments are cropped to the imaging field of view, temporally resampled to 16 fps, resized to $256 \times 256$, and divided into non-overlapping 3-second chunks of 45 frames each; segments shorter than 3 seconds are discarded. This yields 153,892 training clips: abdomen (106,990), cardiac (26,095), and thyroid (20,807), totaling 6,925,140 frames. These clips are used to train the latent-action video model and the foundational video diffusion model. For validation, we hold out 500 clips: 64 thyroid clips together with 218 liver and 218 cardiac clips.

**EM-tracked thyroid ultrasound videos.** To condition the model on the probe motion, we collect thyroid ultrasound scans with synchronized 6-DoF pose measurements using a dual-sensor electromagnetic (EM) tracking system. One sensor is mounted on the probe handle and the second on the patient, allowing probe motion to be expressed relative to the subject rather than the field generator. Each scan follows a fixed acquisition protocol covering three translational and three rotational degrees of freedom. While actions are represented in full 6-DoF, surface-normal translation is physically constrained by probe–skin contact and tissue compression, so freehand scanning effectively explores a contact-constrained subset of the 6-DoF pose space. The dataset contains EM-tracked scans from 42 distinct subjects, split at the subject level into 33 for training and 9 for validation, with no subject overlap. Videos are cropped to the ultrasound field of view, resampled to 16 fps, and resized to $256 \times 256$. Each scan is cut into non-overlapping 45-frame windows, and every rollout is conditioned on the first latent frame of its window plus a 6-DoF action sequence.

## 4.2 Results on Ultrasound World Model Controllability

To assess whether SonoWorld responds to commanded probe motion rather than merely extrapolating plausible video dynamics, we evaluate it under four complementary action settings. **Original pose** replays the measured probe trajectory and measures in-distribution action-following fidelity. **Zero motion** feeds an all-zero action sequence, so the rollout should stay on the initial frame with only physiological motion. **Speed** $\times 2$ subsamples the trajectory by a factor of two, approximately doubling the displacement per step and testing whether the model responds to the commanded motion magnitude rather than a characteristic training-time velocity. **Round trip** follows the measured forward trajectory and then appends the exact inverse motion in reverse temporal order. This setting tests whether pose-conditioned generation remains stable over an extended trajectory that returns to the initial probe pose. For each setting, we quantify generation fidelity using PSNR, SSIM, and LPIPS against original sequence, reported as mean $\pm$ standard deviation over evaluation clips.

Table 1 evaluates whether SonoWorld follows the commanded probe trajectory rather than merely producing plausible ultrasound dynamics. Under **Original pose**, the generated sequence is com-

Table 1: Quantitative controllability evaluation on EM-tracked scans. Ground-truth sequence is generated from original sequence according to the specific task. For zero motion it is the first image.

| Models | Tasks | PSNR ↑ | SSIM ↑ | LPIPS ↓ |
|---|---|---|---|---|
| Bidirectional | Original pose | 16.84±1.17 | 0.402±0.060 | 0.413±0.056 |
| | Zero motion | 16.87±1.12 | 0.385±0.066 | 0.392±0.076 |
| | Speed×2 | 16.89±0.98 | 0.414±0.053 | 0.411±0.051 |
| | Round trip | 16.41±1.09 | 0.376±0.059 | 0.431±0.054 |
| Causal | Original pose | 16.09±0.95 | 0.386±0.054 | 0.439±0.044 |
| | Zero motion | 17.76±1.13 | 0.409±0.062 | 0.390±0.065 |
| | Speed×2 | 16.10±1.05 | 0.388±0.051 | 0.445±0.048 |
| | Round trip | 15.17±0.83 | 0.349±0.044 | 0.465±0.041 |

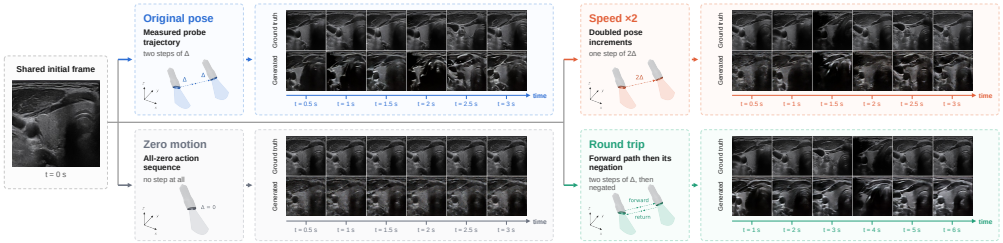


Figure 4: Visualizations on video generation of our ultrasound world model. We utilize the causal model to autoregressively generate future frames conditioned on the same initial ultrasound frame (t=0s) and different probe trajectories.

pared with the observations acquired along the measured trajectory; thus, PSNR, SSIM, and LPIPS quantify how accurately the model reproduces the image evolution induced by real probe motion. The causal model remains close to the bidirectional teacher, with only a 0.75 dB decrease in PSNR, a 0.016 decrease in SSIM, and a 0.026 increase in LPIPS, indicating that causal generation largely preserves pose-conditioned fidelity while enabling streaming inference with four denoising steps. **Zero motion** directly probes null-action stability: setting all 6-DoF actions to zero suppresses probe-induced evolution and all generated observations are substantially near the initial imaging plane, indicating that the generated dynamics respond to the supplied probe actions rather than following an autonomous motion prior. **Speed**$\times 2$ increases the probe displacement per generation step while preserving the underlying trajectory. Both models maintain nearly unchanged reconstruction quality, showing that the predicted image evolution scales with the commanded motion magnitude rather than a fixed temporal or motion prior. **Round trip** further tests whether the learned action representation is approximately reversible: after following the forward trajectory, the model is driven by the reversed actions in negated order. This is the most challenging setting, with PSNR decreasing by 0.43 dB for the bidirectional model and 0.92 dB for the causal model. The larger degradation of the causal model is consistent with error accumulation over the longer autoregressive rollout (23 versus 12 latent frames), while its retained fidelity indicates that learned control remains effective over extended bidirectional motion. We further evaluate axis-specific controllability using synthetic actions that vary one degree of freedom while holding the others fixed in Appendix Fig. 9.

### 4.3 Effect of Pretraining with Latent Actions

We evaluate whether latent actions provide a effective conditioning signal for learning ultrasound dynamics from the large multi-organ corpus, where probe poses are unavailable. We compare two models with the same Wan2.1-T2V-1.3B backbone and training recipe, differing only in whether the learned 32-dimensional latent action is injected through adaptive layer normalization during training and inference. Evaluation is performed on an organ-balanced held-out set of 500 clips, where each rollout is conditioned on the first three latent frames and generates the remaining nine. As shown in Table 2, latent-action conditioning improves PSNR by 3.60 dB and SSIM by 0.083, while reducing LPIPS by 0.067. The substantial and consistent improvements across all three metrics demonstrate the effectiveness of latent-action conditioning in learning ultrasound video dynamics, showing that the learned latent actions capture transition-relevant information that substantially reduces the ambiguity of future observations from visual context alone.

Table 2: Effect of latent actions on ultrasound video diffusion model pretraining.

| Methods | PSNR ↑ | SSIM ↑ | LPIPS ↓ |
|---|---|---|---|
| w/o latent actions | 17.78±2.59 | 0.613±0.110 | 0.266±0.087 |
| w/ latent actions | **21.38±2.80** | **0.696±0.108** | **0.199±0.072** |

### 4.4 Ablation Studies on Causal Model Training Methods

A practical interactive world model must generate observations causally as probe actions arrive, while remaining stable over autoregressive rollouts. Converting the bidirectional model to causal generation therefore introduces a central training challenge: errors in generated context can accumulate over time, and the choice of causal training strategy directly determines long-horizon rollout quality. We compare several causal training strategies under a controlled setting. All causal variants are initialized from the same post-trained bidirectional model, trained on the same 33 EM-tracked scans, and differ only in how the causal context is constructed during training. We evaluate 8-second rollouts (129 image frames; 33 latent frames) conditioned on an initial frame and the measured 6-DoF probe trajectory, with the bidirectional model included as a non-causal reference. As shown in Table 3, self-forcing (Huang et al., 2026b) achieves the best perceptual quality among causal variants, with SSIM $0.394$ and LPIPS $0.436$, while remaining within $0.15$ dB PSNR of the bidirectional reference. Teacher forcing yields slightly higher PSNR ($16.44$ dB) but substantially worse LPIPS ($0.515$), while diffusion, rolling, and reward forcing degrade more consistently across metrics. These results indicate that exposing the model to its own generated context during training better matches the autoregressive inference distribution and preserves visual fidelity over long causal rollouts.

Table 3: Comparison of causal model training methods on 8 second rollouts. For each metric, the best result among causal methods is shown in boldface and the second best is underlined.

| Methods | PSNR ↑ | SSIM ↑ | LPIPS ↓ |
|---|---|---|---|
| Bidirectional Model | 16.52±0.93 | 0.389±0.061 | 0.422±0.051 |
| Teacher Forcing (Gao et al., 2024a) | **16.44±0.76** | <u>0.387±0.044</u> | 0.515±0.055 |
| Diffusion Forcing (Chen et al., 2024) | 16.22±0.81 | 0.373±0.039 | 0.525±0.046 |
| Rolling Forcing (Liu et al., 2026) | 15.77±0.90 | 0.372±0.055 | <u>0.456±0.047</u> |
| Reward Forcing (Lu et al., 2026) | 15.60±0.81 | 0.371±0.051 | 0.469±0.041 |
| **SonoWorld (Ours)** | <u>16.37±0.98</u> | **0.394±0.052** | **0.436±0.047** |

### 4.5 Ablation Studies on Causal Inference Techniques

Long-horizon causal generation requires efficient management of temporal context. Retaining the full KV cache preserves all history but causes memory and attention cost to grow with rollout length, limiting scalable interactive inference. We therefore study whether a bounded cache can retain the information necessary for generation while reducing this cost. We apply different latent-frame-level KV-cache policies at inference time to the same self-forcing model, with no retraining, and evaluate 8-second rollouts containing 33 latent frames. **Full KV** retains all 33 frames (self-forcing default setting); **Local** keeps only the 12 most recent; **Sink+Local** retains 3 initial frames together with the 12 most recent (Xiao et al., 2024); and **Eviction+Local** keeps 8 intermediate frames and the 4 most recent, where intermediate frames are selected either uniformly or by accumulated attention mass (Zhang et al., 2023). As shown in Table 4, all bounded-cache variants remain within $0.14$ dB PSNR, $0.007$ SSIM, and $0.004$ LPIPS of full attention, despite retaining as few as 12 of 33 frames. SonoWorld with selective eviction achieves the best PSNR ($16.37$) and SSIM ($0.394$), while matching the best LPIPS ($0.436$). These results indicate that long-range context is useful but need not be retained densely: selecting informative historical frames can preserve generation quality while substantially reducing cache size and per-step attention cost.

Table 4: Results on KV-cache configurations at inference time. We conducted causal rollouts of 8 second ultrasound videos conditioned on an initial frame and 6 DoF poses.

| Cache Config. | PSNR ↑ | SSIM ↑ | LPIPS ↓ |
|---|---|---|---|
| Full KV | 16.23±0.93 | 0.390±0.049 | 0.437±0.046 |
| Local | 16.26±0.86 | 0.387±0.049 | 0.440±0.045 |
| Sink+Local | 16.31±0.96 | 0.391±0.051 | **0.436±0.048** |
| Eviction (strided)+Local | 16.27±0.94 | 0.391±0.051 | 0.437±0.047 |
| **SonoWorld (Ours)** | **16.37±0.98** | **0.394±0.052** | **0.436±0.047** |

## 5 Applications of Ultrasound World Model

### 5.1 Interactive Application

A practical ultrasound world model should provide plausible and anatomically consistent feedback under interactive probe control, enabling applications such as robotic policy evaluation, operator training, and exploration of probe–anatomy relationships. Because counterfactual probe trajectories often lack paired ground-truth videos, pixel-level reconstruction metrics alone are insufficient to assess such rollouts. We therefore conduct a user study with five experienced ultrasound raters

on 55 generated clips, evaluating three complementary criteria: **image quality**, **video consistency**, and **probe–anatomy alignment**. We evaluate two settings. First, the initial frame is fixed while the probe follows three distinct trajectories (Path A–C), testing whether different actions induce coherent, path-dependent observations. Second, the probe trajectory is fixed while the conditioning frame is shifted laterally from the thyroid midline, with negative $\delta x$ corresponding to the left lobe and positive $\delta x$ to the right lobe. As shown in Table 5, probe–anatomy alignment consistently receives the highest scores, followed by video consistency, while image quality receives relatively lower scores. These results indicate that SonoWorld maintains anatomically aligned and temporally consistent ultrasound observations across different probe trajectories and initial views, even when image fidelity is imperfect, which further confirms SonoWorld can closely follow the probe action.

Table 5: **Human evaluation of pose-conditioned rollouts.** Five experienced ultrasound raters scored 55 generated clips on three 5-point scales (1 = worst, 3=acceptable, 5 = perfect): image quality, video consistency, and probe–anatomy alignment. Values are mean $\pm$ 95% CI over conditioning frames, after averaging raters within each clip.

| | Image quality | Video consistency | Probe–anatomy alignment |
|---|---|---|---|
| *(a) Probe scan path varies; conditioning frame held fixed* | | | |
| Path A | $3.15 \pm 0.19$ | $3.83 \pm 0.26$ | $4.08 \pm 0.35$ |
| Path B | $3.35 \pm 0.23$ | $3.70 \pm 0.36$ | $3.73 \pm 0.40$ |
| Path C | $3.60 \pm 0.25$ | $3.80 \pm 0.13$ | $3.92 \pm 0.18$ |
| *(b) Conditioning frame shifted laterally; path held fixed* | | | |
| $\delta x = -2$ (left lobe) | $3.58 \pm 0.23$ | $4.12 \pm 0.12$ | $4.35 \pm 0.21$ |
| $\delta x = -1$ (left lobe) | $3.40 \pm 0.33$ | $3.85 \pm 0.32$ | $4.25 \pm 0.21$ |
| $\delta x = 0$ (middle) | $3.15 \pm 0.19$ | $3.83 \pm 0.26$ | $4.08 \pm 0.35$ |
| $\delta x = +1$ (right lobe) | $3.12 \pm 0.20$ | $3.65 \pm 0.08$ | $3.48 \pm 0.37$ |
| $\delta x = +2$ (right lobe) | $3.11 \pm 0.28$ | $3.60 \pm 0.26$ | $3.31 \pm 0.43$ |

### 5.2 Model-Based Action Selection

SonoWorld can support robotic navigation only if its predicted futures are sufficiently action-sensitive. We therefore evaluate the world model as an action-scoring mechanism for goal-directed navigation. Given an initial ultrasound frame and a target frame from a held-out tracked scan, we construct two equal-magnitude candidate trajectories along a single degree of freedom: one toward the target pose and one in the opposite direction. SonoWorld generates the terminal observation for each candidate, and PSNR to the target frame serves as the reward. A trial is successful when the action toward the true target receives the higher reward. Across held-out scans, SonoWorld achieves success rates of 74.8% and 66.7% at displacement thresholds of 15 and 20, respectively, indicating that its predicted observations contain action-dependent information that can be used to discriminate between candidate probe motions relative to a target view.

Table 6: Results on model-based action discrimination. Entries are success rates (%), the fraction of rollouts in which the action reconstructs the goal frame more accurately than its negation;

| Threshold | $x$ | $y$ | $r_x$ | $r_y$ | $r_z$ | Avg. |
|---|---|---|---|---|---|---|
| 15 | 73.91 | 78.26 | 61.54 | 86.96 | 66.67 | 74.76 |
| 20 | 88.89 | 77.78 | 66.67 | 77.78 | 44.44 | 66.67 |

## 6 Conclusion

We present SonoWorld, a causal, pose-controllable ultrasound world model that generates future observations conditioned on metric 6-DoF probe motion. SonoWorld learns ultrasound dynamics from around 6.9 million unlabeled clinical ultrasound video frames, grounds them to physical probe actions using a small set of EM-tracked freehand scans, and is distilled into an autoregressive generator with bounded KV-cache inference. Although action grounding is evaluated on thyroid ultrasound, the SonoWorld framework is not organ-specific and can, in principle, be extended to other anatomical regions, such as abdominal organs, given appropriate tracked data for action grounding. Together, these results demonstrate the potential of SonoWorld as a data-driven interactive environment for robotic ultrasound acquisition and policy evaluation. It is worth noticing probe pose also does not fully determine ultrasound appearance: tissue deformation, physiological motion remain unobserved factors, indicating the limitation of this work. The absence of a shared public benchmark also prevents a direct quantitative comparison with the closest action-conditioned ultrasound world model, motivating standardized tracked-ultrasound benchmarks in future work.

## REFERENCES


Eloi Alonso, Adam Jelley, Vincent Micheli, Anssi Kanervisto, Amos Storkey, Tim Pearce, and François Fleuret. Diffusion for world modeling: Visual details matter in Atari. In *Advances in Neural Information Processing Systems*, 2024.

Samy Bengio, Oriol Vinyals, Navdeep Jaitly, and Noam Shazeer. Scheduled sampling for sequence prediction with recurrent neural networks. In *Advances in Neural Information Processing Systems*, volume 28, pp. 1171–1179, 2015.

Jake Bruce, Michael Dennis, Ashley Edwards, Jack Parker-Holder, Yuge Shi, et al. Genie: Generative interactive environments. In *Proceedings of the 41st International Conference on Machine Learning*, 2024.

Benny Bürger, Sascha Bettinghausen, Matthias Rädle, and Jürgen Hesser. Real-time GPU-based ultrasound simulation using deformable mesh models. *IEEE Transactions on Medical Imaging*, 32(3):609–618, 2013.

Boyuan Chen, Diego Martí Monsó, Yilun Du, Max Simchowitz, Russ Tedrake, and Vincent Sitzmann. Diffusion forcing: Next-token prediction meets full-sequence diffusion. *Advances in Neural Information Processing Systems*, 37:24081–24125, 2024.

Jingtao Ding, Yunke Zhang, Yu Shang, Yuheng Zhang, Zefang Zong, Jie Feng, Yuan Yuan, Hongyuan Su, Nian Li, Nicholas Sukiennik, et al. Understanding world or predicting future? a comprehensive survey of world models. *ACM Computing Surveys*, 58(3):1–38, 2025.

Haiyan Du, Xinran Zhang, Yongde Zhang, Fujun Zhang, Letao Lin, and Tao Huang. A review of robot-assisted ultrasound examination: Systems and technology. *The International Journal of Medical Robotics and Computer Assisted Surgery*, 20(4):e2660, 2024. doi: 10.1002/rcs.2660.

Siqi Fan, Mingcong Chen, Ran Liu, Zixuan Yang, Xiaoyu Fu, Xiaoqing Gao, Yunhui Liu, and Hongbin Liu. Action-conditioned world model for goal plane probe guidance in robotic ultrasound. *arXiv preprint arXiv:2607.21918*, 2026.

Hang Gao, Hon Fai Choi, Piet Claus, Steven Boonen, Siegfried Jaecques, G. Harry Van Lenthe, Georges Van der Perre, Walter Lauriks, and Jan D'hooge. A fast convolution-based methodology to simulate 2-D/3-D cardiac ultrasound images. *IEEE Transactions on Ultrasonics, Ferroelectrics, and Frequency Control*, 56(2):404–409, 2009.

Kaifeng Gao, Jiaxin Shi, Hanwang Zhang, Chunping Wang, Jun Xiao, and Long Chen. Ca2-vdm: Efficient autoregressive video diffusion model with causal generation and cache sharing. *arXiv preprint arXiv:2411.16375*, 2024a.

Shenyuan Gao, Jiazhi Yang, Li Chen, Kashyap Chitta, Yihang Qiu, Andreas Geiger, Jun Zhang, and Hongyang Li. Vista: A generalizable driving world model with high fidelity and versatile controllability. *Advances in Neural Information Processing Systems*, 37:91560–91596, 2024b.

Shenyuan Gao, Siyuan Zhou, Yilun Du, Jun Zhang, and Chuang Gan. AdaWorld: Learning adaptable world models with latent actions. In *Proceedings of the 42nd International Conference on Machine Learning*, volume 267, pp. 18744–18771. PMLR, 2025.

Shenyuan Gao, William Liang, Kaiyuan Zheng, Ayaan Malik, Seonghyeon Ye, et al. DreamDojo: A generalist robot world model from large-scale human videos. *arXiv preprint arXiv:2602.06949*, 2026a.

Sicong Gao, Maurice Pagnucco, Tomasz Bednarz, and Yang Song. Nvidia isaac sim: Enabling scalable, gpu-accelerated simulation for robotics. *arXiv preprint arXiv:2606.03551*, 2026b.

Bohan Hou, Gen Li, Jindou Jia, Tuo An, Xinying Guo, Sicong Leng, Haoran Geng, Yanjie Ze, Tatsuya Harada, Philip Torr, et al. World model for robot learning: A comprehensive survey. *arXiv preprint arXiv:2605.00080*, 2026.

Anthony Hu, Lloyd Russell, Hudson Yeo, Zak Murez, George Fedoseev, Alex Kendall, Jamie Shotton, and Gianluca Corrado. GAIA-1: A generative world model for autonomous driving. *arXiv preprint arXiv:2309.17080*, 2023.

Siqiao Huang, Jialong Wu, Qixing Zhou, Shangchen Miao, and Mingsheng Long. Vid2world: Crafting video diffusion models to interactive world models. In *The Fourteenth International Conference on Learning Representations*, 2026a.

Xun Huang, Zhengqi Li, Guande He, Mingyuan Zhou, and Eli Shechtman. Self forcing: Bridging the train-test gap in autoregressive video diffusion. *Advances in Neural Information Processing Systems*, 38:167283–167308, 2026b.

Joel Jang, Seonghyeon Ye, Zongyu Lin, Jiannan Xiang, Johan Bjorck, et al. DreamGen: Unlocking generalization in robot learning through video world models. *arXiv preprint arXiv:2505.12705*, 2025.

Jiri Jaros, Alistair P Rendell, and Bradley E Treeby. Full-wave nonlinear ultrasound simulation on distributed clusters with applications in high-intensity focused ultrasound. *The International Journal of High Performance Computing Applications*, 30(2):137–155, 2016.

Haojun Jiang, Meng Li, Zhenguo Sun, Ning Jia, Yu Sun, Shaqi Luo, Shiji Song, and Gao Huang. Structure-aware world model for probe guidance via large-scale self-supervised pre-train. In *International Workshop on Advances in Simplifying Medical Ultrasound (ASMUS)*, pp. 58–67. Springer, 2024a.

Haojun Jiang, Zhenguo Sun, Ning Jia, Meng Li, Yu Sun, Shaqi Luo, Shiji Song, and Gao Huang. Cardiac copilot: Automatic probe guidance for echocardiography with world model. In *Medical Image Computing and Computer-Assisted Intervention (MICCAI)*, pp. 190–199. Springer, 2024b.

Haojun Jiang, Anyu Zhao, Qingqing Yang, Xiaoxiao Yan, Taiyu Wang, Yulin Wang, Ning Jia, Jiangshan Wang, Gaofeng Wu, Yang Yue, Shaqi Luo, Hanwen Wang, Long Ren, Shiji Chen, Pan Liu, Guoquan Yao, Wenbo Yang, Shiji Song, Xiang Li, Kaiqing He, and Gao Huang. Towards expert-level autonomous carotid ultrasonography with large-scale learning-based robotic system. *Nature Communications*, 16(1):7893, 2025.

Zhongliang Jiang, Septimiu E. Salcudean, and Nassir Navab. Robotic ultrasound imaging: State-of-the-art and future perspectives. *Medical Image Analysis*, 89:102878, 2023. doi: 10.1016/j.media.2023.102878.

Anssi Kanervisto, Dave Bignell, Linda Yilin Wen, Martin Grayson, Raluca Georgescu, et al. World and human action models towards gameplay ideation. *Nature*, 638:656–663, 2025.

Saurabh Koju, Saurav Bastola, Prashant Shrestha, Sanskar Amgain, Yash Raj Shrestha, Rudra P. K. Poudel, and Binod Bhattarai. Surgical vision world model. In *MICCAI Workshop on Data Engineering in Medical Imaging*, pp. 1–10. Springer, 2025.

Andras Lasso, Tamas Heffter, Adam Rankin, Csaba Pinter, Tamas Ungi, and Gabor Fichtinger. PLUS: Open-source toolkit for ultrasound-guided intervention systems. *IEEE Transactions on Biomedical Engineering*, 61(10):2527–2537, 2014.

Chenxin Li, Hengyu Liu, Yifan Liu, Brandon Y. Feng, Wuyang Li, Xinyu Liu, Zhen Chen, Jing Shao, and Yixuan Yuan. Endora: Video generation models as endoscopy simulators. In *Medical Image Computing and Computer Assisted Intervention (MICCAI)*, volume 15006, pp. 230–240. Springer, 2024.

Yaron Lipman, Ricky T. Q. Chen, Heli Ben-Hamu, Maximilian Nickel, and Matt Le. Flow matching for generative modeling. In *International Conference on Learning Representations*, 2023.

Kunhao Liu, Wenbo Hu, Jiale Xu, Ying Shan, and Shijian Lu. Rolling forcing: Autoregressive long video diffusion in real time. In *International Conference on Learning Representations*, volume 2026, pp. 91177–91196, 2026.

Xingchao Liu, Chengyue Gong, and Qiang Liu. Flow straight and fast: Learning to generate and transfer data with rectified flow. In *International Conference on Learning Representations*, 2023.

Yunhong Lu, Yanhong Zeng, Haobo Li, Hao Ouyang, Qiuyu Wang, Ka Leong Cheng, Jiapeng Zhu, Hengyuan Cao, Zhipeng Zhang, Xing Zhu, et al. Reward forcing: Efficient streaming video generation with rewarded distribution matching distillation. In *Proceedings of the IEEE/CVF Conference on Computer Vision and Pattern Recognition*, pp. 34385–34397, 2026.

NVIDIA, Niket Agarwal, Arslan Ali, Maciej Bala, Yogesh Balaji, et al. Cosmos world foundation model platform for physical AI. *arXiv preprint arXiv:2501.03575*, 2025.

Sanjeev Rapuri, Lalithkumar Seenivasan, Daniel Schneider, Roger Soberanis-Mukul, Yuxin He, and Mathias Unberath. SAW: Toward a surgical action world model via controllable and scalable video generation. *arXiv preprint arXiv:2603.13024*, 2026.

Mehrdad Salehi, Seyed-Ahmad Ahmadi, Raphael Prevost, Nassir Navab, and Wolfgang Wein. Patient-specific 3D ultrasound simulation based on convolutional ray-tracing and appearance optimization. In *Medical Image Computing and Computer-Assisted Intervention (MICCAI)*. Springer, 2015.

Ramtin Shams, Richard Hartley, and Nassir Navab. Real-time simulation of medical ultrasound from CT images. In *Medical Image Computing and Computer-Assisted Intervention (MICCAI)*, pp. 734–741. Springer, 2008.

Kang Su, Jingwei Liu, Xiaoqi Ren, Yingxiang Huo, Guanglong Du, Wei Zhao, Xueqian Wang, Bin Liang, Di Li, and Peter X. Liu. A fully autonomous robotic ultrasound system for thyroid scanning. *Nature Communications*, 15(1):4004, 2024.

Santiago Vitale, José Ignacio Orlando, Emmanuel Iarussi, and Ignacio Larrabide. Improving realism in patient-specific abdominal ultrasound simulation using CycleGANs. *International Journal of Computer Assisted Radiology and Surgery*, 15(2):183–192, 2020.

Team Wan, Ang Wang, Baole Ai, Bin Wen, Chaojie Mao, Chen-Wei Xie, Di Chen, Feiwu Yu, Haiming Zhao, Jianxiao Yang, et al. Wan: Open and advanced large-scale video generative models. *arXiv preprint arXiv:2503.20314*, 2025.

Shiying Wang, John A Hossack, and Alexander L Klibanov. From anatomy to functional and molecular biomarker imaging, and therapy: ultrasound is safe, ultrafast, portable, and inexpensive. *Investigative radiology*, 55(9):559, 2020.

Guangxuan Xiao, Yuandong Tian, Beidi Chen, Song Han, and Mike Lewis. Efficient streaming language models with attention sinks. In *International Conference on Learning Representations*, volume 2024, pp. 21875–21895, 2024.

Jingjing Xu, Xu Sun, Zhiyuan Zhang, Guangxiang Zhao, and Junyang Lin. Understanding and improving layer normalization. *Advances in neural information processing systems*, 32, 2019.

Jiazhi Yang, Kashyap Chitta, Shenyuan Gao, Long Chen, Yuqian Shao, Xiaosong Jia, Hongyang Li, Andreas Geiger, Xiangyu Yue, and Li Chen. ReSim: Reliable world simulation for autonomous driving. In *Advances in Neural Information Processing Systems*, 2025.

Mengjiao Yang, Yilun Du, Kamyar Ghasemipour, Jonathan Tompson, Dale Schuurmans, and Pieter Abbeel. Learning interactive real-world simulators. In *International Conference on Learning Representations*, 2024.

Seonghyeon Ye, Joel Jang, Byeongguk Jeon, Sejune Joo, Jianwei Yang, et al. Latent action pretraining from videos. In *International Conference on Learning Representations*, 2025.

Tianwei Yin, Michaël Gharbi, Richard Zhang, Eli Shechtman, Fredo Durand, William T Freeman, and Taesung Park. One-step diffusion with distribution matching distillation. In *Proceedings of the IEEE/CVF Conference on Computer Vision and Pattern Recognition*, pp. 6613–6623, 2024.

Yang Yue, Yulin Wang, Haojun Jiang, Pan Liu, Shiji Song, and Gao Huang. Echoworld: Learning motion-aware world models for echocardiography probe guidance. In *2025 IEEE/CVF Conference on Computer Vision and Pattern Recognition (CVPR)*, pp. 25993–26003. IEEE, 2025.

Zhenyu Zhang, Ying Sheng, Tianyi Zhou, Tianlong Chen, Lianmin Zheng, Ruisi Cai, Zhao Song, Yuandong Tian, Christopher Ré, Clark Barrett, et al. H2o: Heavy-hitter oracle for efficient generative inference of large language models. *Advances in neural information processing systems*, 36:34661–34710, 2023.

### AI USE STATEMENT

Generative AI assisted manuscript drafting, editing, literature and code inspection.

### ETHICS STATEMENT

This study was conducted under institutional review board (IRB) approval and in accordance with the applicable requirements for research involving human data. Clinical ultrasound data were handled under the approved protocol and de-identified prior to research use. The EM-tracked ultrasound acquisition and expert evaluation were conducted under the corresponding approved procedures. We do not release identifiable clinical data, and all reported results are presented in aggregate.

### REPRODUCIBILITY STATEMENT

We document data collection, splits and sampling, training settings, and evaluation protocols.

## A APPENDIX

### A.1 LIMITATION OF SONOWORLD

SonoWorld currently grounds physical actions using a relatively small thyroid-only EM-tracked cohort, and its learned dynamics are therefore validated only within the action and anatomical distributions represented by these data. Probe pose also does not fully determine ultrasound appearance: contact force, tissue deformation, physiological motion, and scanner settings remain unobserved factors. Pixel-level metrics such as PSNR, SSIM, and LPIPS provide only indirect evidence of geometric control, and null-action rollouts exhibit. In addition, the lack of a shared tracked-ultrasound benchmark prevents a direct quantitative comparison with the closest action-conditioned ultrasound world models. SonoWorld should therefore be viewed as a learned, data-driven environment rather than a physically guaranteed ultrasound simulator.

### A.2 DETAILED DERIVATION FOR POSE CALIBRATION AND RELATIVE POSE CONVERSION

This appendix expands Eqs. equation 2–equation 4. Throughout, $t$ indexes tracker samples rather than diffusion time.

**Notation and pose convention.** Each scan records two synchronized EM streams: a sensor clamped to the probe handle and a second sensor taped to the patient, whose only purpose is to measure patient motion. Each stream provides, per sample $t$, a timestamp, a unit quaternion $\mathbf{q}_t = (w, x, y, z)$, a position $\mathbf{p}_t \in \mathbb{R}^3$ in millimetres, and a scalar tracking quality $\kappa_t$. All geometry uses homogeneous $4 \times 4$ transforms in the canonical column-vector convention,

$$\mathbf{T} = \begin{bmatrix} \mathbf{R} & \mathbf{p} \\ \mathbf{0}^\top & 1 \end{bmatrix} \in SE(3), \qquad \tilde{\mathbf{x}}_{\text{target}} = \mathbf{T}\,\tilde{\mathbf{x}}_{\text{source}}, \qquad \mathbf{T}^{-1} = \begin{bmatrix} \mathbf{R}^\top & -\mathbf{R}^\top\mathbf{p} \\ \mathbf{0}^\top & 1 \end{bmatrix}, \tag{5}$$

with $\tilde{\mathbf{x}} = [\mathbf{x}^\top, 1]^\top$ and the product $\mathbf{T}_A\mathbf{T}_B$ meaning $A$ applied after $B$. We write $\mathbf{T}_{B\leftarrow A}$ for the transform taking coordinates in frame $A$ to frame $B$, so that transforms compose by matching adjacent subscripts, $\mathbf{T}_{C\leftarrow A} = \mathbf{T}_{C\leftarrow B}\mathbf{T}_{B\leftarrow A}$.

The mapping from the stored quaternion to a rotation matrix carries two binary ambiguities: whether $w$ is stored first or last, and whether $\mathbf{R}$ maps sensor to world or world to sensor. We measure rather than assume them. All four combinations are scored by how well the sensor origin traces a sphere about a fixed pivot, and the winner is decided by majority vote over up to eight scans, since the

layout is a property of the recording software and cannot vary per scan. On this corpus the detected convention is $w$-first with a transpose, that is

$$\mathbf{x}_{\text{world}} = \mathbf{R}(\mathbf{q}_t)\,\mathbf{x}_{\text{sensor}} + \mathbf{p}_t, \qquad \mathbf{T}_{\text{world}\leftarrow\text{sensor}}(t) = \big[\mathbf{R}(\mathbf{q}_t) \mid \mathbf{p}_t\big]. \tag{6}$$

**From sensor pose to probe-tip pose.** The tracked sensor sits on the probe handle, roughly $119$ mm from the acoustic tip, whereas the imaging plane is attached to the tip. The two frames are rigidly connected, so a constant offset, the lever arm, must be composed onto every sample. The manufacturer supplies a probe-to-sensor matrix $\mathbf{M}_{\text{P2S}}$; converting it into the frame our files use requires two signed axis relabellings,

$$\mathbf{T}_{\text{sensor}\leftarrow\text{tip}} = \mathbf{A}_{\text{file}\leftarrow\text{vendor}}\;\mathbf{M}_{\text{P2S}}\;\mathbf{A}^{-1}_{\text{tip}\leftarrow\text{probe}}, \tag{7}$$

where each $\mathbf{A}$ is a signed permutation matrix with determinant $+1$, so that the relabelling stays right-handed. For the thyroid probe, $\mathbf{A}_{\text{file}\leftarrow\text{vendor}} : (x, y, z) \mapsto (-Y, -Z, +X)$, selected by scoring all $48$ signed axis permutations against the tracking data, and $\mathbf{A}_{\text{tip}\leftarrow\text{probe}} : (x, y, z) \mapsto (-Y, +Z, -X)$, which names the tip frame as (transverse, transverse, axial) with the axial axis pointing from the sensor toward the tip. Writing $\mathbf{T}_{\text{sensor}\leftarrow\text{tip}} = [\mathbf{R}_{\text{st}} \mid \mathbf{r}]$, the translation $\mathbf{r}$ is the tip position in sensor coordinates, with $\|\mathbf{r}\| \approx 119.2$ mm for the thyroid probe, and $\mathbf{R}_{\text{st}}$ is the probe frame. The delivered thyroid matrix carries a $1.7^\circ$ tilt away from an exact axis permutation, so it is a measured calibration rather than a CAD ideal; the cardiac and abdomen probes are exact $90^\circ$ turns about the sensor $z$ axis.

**Two-sensor composition.** Let $\mathbf{T}^{\text{probe}}_{\text{world}\leftarrow\text{sensor}}(t)$ and $\mathbf{T}^{\text{ref}}_{\text{world}\leftarrow\text{sensor}}(t)$ be the probe- and patient-sensor poses in the world frame of the field generator. The quantity of interest is the tip pose expressed in the patient frame, which factorizes uniquely as Eq. equation 2,

$$\mathbf{T}_{\text{patient}\leftarrow\text{tip}}(t) = \big(\mathbf{T}^{\text{ref}}_{\text{world}\leftarrow\text{sensor}}(t)\big)^{-1}\,\mathbf{T}^{\text{probe}}_{\text{world}\leftarrow\text{sensor}}(t)\,\mathbf{T}_{\text{sensor}\leftarrow\text{tip}}. \tag{8}$$

The order is forced by the frame in which each factor is written: $\mathbf{T}_{\text{sensor}\leftarrow\text{tip}}$ multiplies on the right because it is expressed in the probe-sensor frame, and $(\mathbf{T}^{\text{ref}}_{\text{world}\leftarrow\text{sensor}})^{-1}$ multiplies on the left because it changes the world frame. Abbreviating the blocks as $[\mathbf{R}_{\text{probe},t} \mid \mathbf{p}_{\text{probe},t}]$ and $[\mathbf{R}_{\text{ref},t} \mid \mathbf{p}_{\text{ref},t}]$ and expanding with Eq. equation 5,

$$\mathbf{T}^{\text{probe}}_{\text{world}\leftarrow\text{sensor}}(t)\,\mathbf{T}_{\text{sensor}\leftarrow\text{tip}} = \big[\,\mathbf{R}_{\text{probe},t}\mathbf{R}_{\text{st}} \;\big|\; \mathbf{R}_{\text{probe},t}\mathbf{r} + \mathbf{p}_{\text{probe},t}\,\big], \tag{9}$$

and left-multiplying by $[\mathbf{R}^\top_{\text{ref},t} \mid -\mathbf{R}^\top_{\text{ref},t}\mathbf{p}_{\text{ref},t}]$ gives

$$\mathbf{R}^{\text{tip}}_t = \mathbf{R}^\top_{\text{ref},t}\,\mathbf{R}_{\text{probe},t}\,\mathbf{R}_{\text{st}}, \qquad \mathbf{p}^{\text{tip}}_t = \mathbf{R}^\top_{\text{ref},t}\big(\mathbf{p}_{\text{probe},t} + \mathbf{R}_{\text{probe},t}\mathbf{r} - \mathbf{p}_{\text{ref},t}\big). \tag{10}$$

Both rotations participate: the reference rotation acts on the whole probe-to-reference vector, not only on the tip's orientation. Omitting $\mathbf{R}^\top_{\text{ref},t}$ from the translation, which is the usual form of this error, incurs a discrepancy of the reference rotation times the inter-sensor distance, approximately $130$ mm on this data.

A distant patient sensor injects more error than the patient motion it removes, because its orientation error is multiplied by the inter-sensor baseline and lies almost entirely below $0.5$ Hz, so no zero-phase filter removes it. Reference compensation is therefore applied only when the mean baseline satisfies $\bar{b} \le 300$ mm, and otherwise the tip is left in the world frame,

$$\mathbf{T}^{\text{tip}}_t = \begin{cases} \big(\mathbf{T}^{\text{ref}}_{\text{world}\leftarrow\text{sensor}}(t)\big)^{-1}\mathbf{T}^{\text{probe}}_{\text{world}\leftarrow\text{sensor}}(t)\,\mathbf{T}_{\text{sensor}\leftarrow\text{tip}}, & \bar{b} \le 300\,\text{mm}, \\ \mathbf{T}^{\text{probe}}_{\text{world}\leftarrow\text{sensor}}(t)\,\mathbf{T}_{\text{sensor}\leftarrow\text{tip}}, & \text{otherwise.} \end{cases} \tag{11}$$

On the 42 retained EM thyroid segments this yields 35 patient-referenced and 7 world-frame segments.

**World-frame poses to egocentric relative poses.** The action must describe what the operator does rather than the orientation and placement of the patient, so absolute world poses are unusable as conditioning: they are not invariant to the transmitter frame. Abbreviating $\mathbf{T}(t) \equiv \mathbf{T}_{\text{patient}\leftarrow\text{tip}}(t) = [\mathbf{R}_t \mid \mathbf{p}_t]$, the pose stream is converted to relative poses expressed in the probe's own frame. For any ordered pair of samples $(s, t)$, Eq. equation 5 gives

$$\mathbf{T}_{s\to t} = \mathbf{T}(s)^{-1}\mathbf{T}(t) = \begin{bmatrix} \mathbf{R}_s^\top & -\mathbf{R}_s^\top\mathbf{p}_s \\ \mathbf{0}^\top & 1 \end{bmatrix}\begin{bmatrix} \mathbf{R}_t & \mathbf{p}_t \\ \mathbf{0}^\top & 1 \end{bmatrix} = \begin{bmatrix} \mathbf{R}_s^\top\mathbf{R}_t & \mathbf{R}_s^\top(\mathbf{p}_t - \mathbf{p}_s) \\ \mathbf{0}^\top & 1 \end{bmatrix}, \tag{12}$$

which is Eq. equation 3. Since $SE(3)$ is not a vector space, the 6-DoF action is the concatenation of the translation block with the rotation vector, that is the axis-angle vector obtained from the $\mathfrak{so}(3)$ logarithm of the rotation block. For $\mathbf{R} \in SO(3)$ with angle $\theta = \arccos\big((\operatorname{tr}\mathbf{R} - 1)/2\big)$,

$$\log(\mathbf{R}) = \frac{\theta}{2\sin\theta}\big(\mathbf{R} - \mathbf{R}^\top\big), \qquad \begin{bmatrix} 0 & -\omega_3 & \omega_2 \\ \omega_3 & 0 & -\omega_1 \\ -\omega_2 & \omega_1 & 0 \end{bmatrix}^\vee = \boldsymbol{\omega}, \tag{13}$$

so that $\log(\mathbf{R})^\vee = \theta\mathbf{u}$ with $\mathbf{u}$ the unit rotation axis. Combining Eqs. equation 12 and equation 13 gives Eq. equation 4,

$$\mathbf{a}_{s\to t} = \big[\ \underbrace{\mathbf{R}_s^\top(\mathbf{p}_t - \mathbf{p}_s)}_{\text{local translation, mm}}\ \big\|\ \underbrace{\log\big(\mathbf{R}_s^\top\mathbf{R}_t\big)^\vee}_{\text{relative rotation, rad}}\ \big] \in \mathbb{R}^6. \tag{14}$$

Two properties matter. First, left-multiplying the whole stream by any fixed world transform, $\mathbf{T}(\cdot) \mapsto \mathbf{G}\mathbf{T}(\cdot)$, leaves $(\mathbf{G}\mathbf{T}(s))^{-1}\mathbf{G}\mathbf{T}(t) = \mathbf{T}(s)^{-1}\mathbf{T}(t)$ unchanged, so the action is invariant to the choice of world frame. Second, the translation is resolved in the local axes of the start anchor, which makes it egocentric: advancing 2 mm along the beam is the same action wherever on the body it occurs. The rotation vector is used rather than a quaternion or Euler angles because it is a continuous, minimal, three-dimensional parameterization with no gimbal lock and no double cover, which is what a regression target requires.

**Chunk-anchored action.** The Wan VAE compresses time by $4\times$ with an independent first frame, so the 45 pixel frames of a clip map to 12 latent frames, with latent frame $i$ anchored at pixel frame $\tau_i = 4i$ for $i = 0, \ldots, 11$. Taking the net motion of each latent frame, $\mathbf{a}_{\tau_{i-1}\to\tau_i}$, would discard the shape of the motion inside it: a smooth 2 mm sweep and a jerk followed by a stop produce the same net displacement. We therefore anchor every pixel frame to the start of its own window instead. For each pixel frame $f = 1, \ldots, 44$, define its chunk anchor and the corresponding action

$$\pi(f) = 4\Big\lfloor \frac{f-1}{4} \Big\rfloor \in \{0, 4, 8, \ldots, 40\}, \qquad \mathbf{a}'_f = \mathbf{a}_{\pi(f)\to f}, \tag{15}$$

so that every frame carries the cumulative motion since the start of its own four-frame window,

$$\underbrace{0{\to}1,\ 0{\to}2,\ 0{\to}3,\ 0{\to}4}_{\text{latent frame 1}},\quad \underbrace{4{\to}5,\ 4{\to}6,\ 4{\to}7,\ 4{\to}8}_{\text{latent frame 2}},\quad \underbrace{8{\to}9,\ \ldots}_{\text{latent frame 3}},\ \ldots \tag{16}$$

yielding $\mathbf{A}' \in \mathbb{R}^{44\times 6}$ with no null row. Grouping the four entries belonging to each latent frame gives $\mathbb{R}^{11\times 24}$, and a zero row is prepended inside the generator for latent frame 0, which has no predecessor, restoring the 12-step alignment. Each group traces the within-chunk trajectory $0 \to 1 \to 2 \to 3 \to 4$ rather than only its endpoint, while its final entry $\mathbf{a}'_{4i}$ is the net motion $\mathbf{a}_{\tau_{i-1}\to\tau_i}$ of that latent frame, so no information is lost relative to the one-vector-per-latent-frame encoding.

**Normalization and quality weighting.** Translation is in millimetres and rotation in radians, quantities that differ by orders of magnitude, so each of the six dimensions is standardized with statistics fitted on the training split only and applied unchanged to evaluation,

$$\tilde{\mathbf{a}}^{(j)} = \frac{\mathbf{a}^{(j)} - \mu_j}{\sigma_j}, \qquad \sigma_j \leftarrow \max(\sigma_j, 10^{-6}). \tag{17}$$

The statistics are fitted over all 44 rows, none of which is a structural zero. Each action step additionally carries a pooled tracking quality $\bar{\kappa}_i$, the mean of $\kappa$ over the frames spanned by that step, and a binary weight $w_i$, set to 1 when $\bar{\kappa}_i < 2000$ and to 0 otherwise, with missing quality treated as usable. Training can therefore mask the steps recorded under weak tracking.

### A.3 Latent Action Model Training

**Architecture of Latent Action Model.** The latent action model (LAM) (Gao et al., 2025) is a conditional variational autoencoder that infers a compact code for the transition between two frames (Fig. 5). Given a source frame $x^i$ and a target frame $x^{i+1}$, each frame is split into non-overlapping patches, giving patch-token sequences $u^i$ and $u^{i+1}$. A learnable action token, $z^i$ or

$z^{i+1}$, is prepended to each sequence. The encoder $E_\phi$ is a spatio-temporal transformer whose blocks alternate spatial attention within each frame with temporal attention across the two frames. Through temporal attention, the action token of the target frame gathers information from the source frame. We keep only this token and discard all patch tokens. A linear head maps this token to the mean $\mu$ and variance $\sigma^2$ of a diagonal Gaussian posterior $q_\phi(z^{i+1} \mid x^i, x^{i+1})$, which yields a low-dimensional latent action $z^{i+1}$. The decoder $D_\psi$ is a spatial-only transformer. It predicts the target frame $\hat{x}^{i+1}$ from the source tokens $u^i$, with $z^{i+1}$ added to every token. Because the decoder never sees $x^{i+1}$, the target frame can reach its own reconstruction only through $z^{i+1}$. The source frame already provides the appearance, so this bottleneck forces $z^{i+1}$ to encode the change between the two frames (probe motion and the resulting anatomical displacement) rather than the anatomy itself.

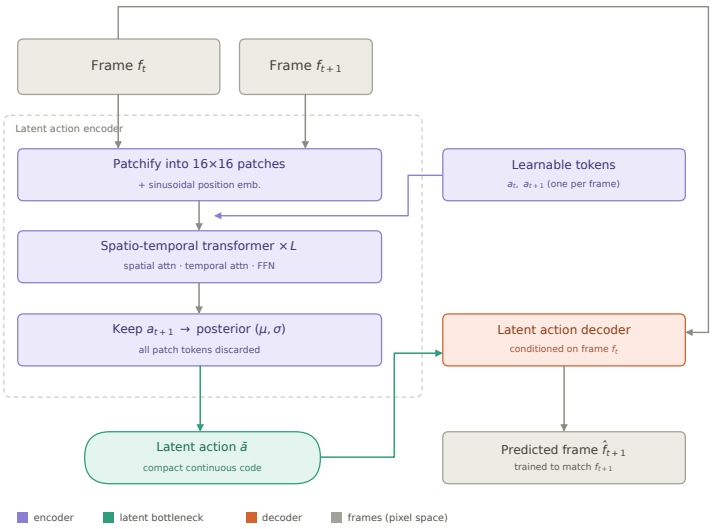


Figure 5: Network architecture of the latent action model.

**Training details.** Training pairs are sampled from clips resampled to 16 fps. The source frame $x^i$ is drawn uniformly from a clip, and the target frame $x^{i+1}$ is taken $\delta \sim \mathcal{U}\{1, \ldots, 4\}$ frames later, so that $z^{i+1}$ captures probe motions of variable duration. Both frames of a pair receive the same random brightness shift. During training, $z^{i+1}$ is sampled with the reparameterization trick, $z^{i+1} = \mu + \sigma \odot \epsilon$ with $\epsilon \sim \mathcal{N}(0, I)$. At inference, we use the posterior mean $z^{i+1} = \mu$. The training objective combines a per-pixel reconstruction loss with a KL regularizer toward a standard normal prior:

$$\mathcal{L}(\phi, \psi) = \mathbb{E}\big[\|x^{i+1} - \hat{x}^{i+1}\|_2^2\big] + \beta\, D_{\mathrm{KL}}\big(q_\phi(z^{i+1} \mid x^i, x^{i+1}) \,\|\, \mathcal{N}(0, I)\big). \tag{18}$$

We set $\beta$ small, so the KL term only keeps the posterior scales well-conditioned. The bottleneck therefore comes mainly from the low dimensionality of $z^{i+1}$ and from the decoder's lack of access to $x^{i+1}$. We monitor PSNR and SSIM of $\hat{x}^{i+1}$ as reconstruction diagnostics. Table 7 lists all hyperparameters.

### A.4 Implementation details

**Pretraining data.** The foundational model is trained on the full 153,892-clip multi-organ corpus, composed of 69.5% abdomen, 17.0% cardiac and 13.5% thyroid clips. Training reads cached latents and cached actions rather than pixels: each clip is stored as a $12 \times 16 \times 32 \times 32$ latent, the Wan VAE encoding of 45 frames at $256 \times 256$, together with its $12 \times 32$ sequence of latent actions, and a per-organ T5 text embedding cached once and looked up by organ label. The VAE, the text encoder and the latent action model are therefore absent from the training loop, which is what makes a 768-clip effective batch affordable. No data augmentation is applied at this stage: at this corpus size the data supplies its own diversity, and caching is the more valuable trade.

**Post-training data and temporal augmentation.** The EM-tracked corpus is three orders of magnitude smaller, 42 tracked thyroid scans yielding 262 clips, which is too few to learn a controllable

Table 7: Hyperparameters of the latent action model.

| Hyperparameter | Value |
|---|---|
| Frame resolution / patch size $p$ | $256 \times 256$ / 16 |
| Patch tokens per frame / token dim. | 256 / 768 |
| Width / attention heads | 1024 / 16 (head dim. 64) |
| Encoder / decoder blocks | 24 / 24 |
| Positional encoding | sinusoidal (spatial), RoPE (temporal) |
| Latent action dim. $d_z$ | 32 |
| KL weight $\beta$ | $10^{-6}$ |
| Frame gap $\delta$ | $\mathcal{U}\{1, \ldots, 4\}$ at 16 fps |
| Brightness jitter | $\mathcal{U}(-0.1,\ 0.1)$, shared within a pair |
| Optimizer | AdamW |
| Learning rate / weight decay | $2.5 \times 10^{-5}$ / $10^{-2}$ |
| Gradient clipping | 0.3 |
| Precision | bf16 |
| Batch size | 128/GPU $\times$ 4 GPUs $= 512$ pairs |
| Training corpus | 153,892 ultrasound clips |
| | (abdomen 69.5% / cardiac 17% / thyroid 13.5%) |

mapping from a 24-dimensional action to nine generated latent frames. We therefore invert the trade made above and do not train on precomputed clips at all. The dataloader reads whole segments, samples a 45-frame window inside the probe-contact interval, applies one temporal augmentation, and VAE-encodes the result on the fly. Every augmentation is expressed as a length-45 integer index array into the source frames; the same index is applied to the pixel frames and to the per-frame tip pose, and the action is recomputed from the indexed pose by the procedure of Section A.2. No per-augmentation action algebra is needed, and the action is correct by construction for any index map. Table 8 lists the four cases, sampled with equal probability.

Table 8: Online temporal augmentation used in post-training. Each case is an index map into the source segment; the action is recomputed from the indexed pose rather than edited.

| Augmentation | Prob. | Index map | Effect on the action |
|---|---|---|---|
| Identity | 0.25 | $[s,\ s+45)$ | unchanged |
| Reverse | 0.25 | $[s+44,\ s]$ descending | motion played backward |
| Stride | 0.25 | $s + \sigma[0, \ldots, 44]$, $\sigma \in \{2, 3\}$ | composed, faster motion |
| Stop-motion | 0.25 | monotonic non-decreasing with repeats | exact zero-motion steps |

Stop-motion freezes a fraction $\rho \sim \mathcal{U}(0.1, 0.35)$ of the 45 output steps by repeating the current frame, which yields action entries that are exactly zero. This is the only mechanism that places a null action inside the training distribution, and it is what teaches the model the correspondence between a zero action and a static image. Stride augmentation requires a longer source window, 133 frames at $\sigma = 3$, which is why segments rather than pre-cut clips are the unit of storage. Because windows and augmentations are resampled online, a pass over the 262 slots does not repeat data: the effective sample space is the set of draws of window start, augmentation and noise.

**Action control via adaptive layer normalization.** The action enters the network only through the linear embedding $\mathbf{a}_i = W_a \mathbf{u}_i + \mathbf{b}_a$ with $W_a \in \mathbb{R}^{d \times d_a}$. Everything downstream of it (the shared projection, the per-block offsets, all transformer blocks and the head) operates at width $d$ and does not depend on the action dimension $d_a$. Switching action spaces therefore requires replacing only this one matrix. During pretraining, $\mathbf{u}_i$ is the 32-dimensional LAM latent action of latent frame $i$, so $d_a = 32$. During post-training, each clip of 45 pixel frames provides 44 per-frame 6-DoF motions, one for every pixel frame after the first, each measured from the start of its four-frame window. The four motions that fall within the same latent frame are concatenated into a single 24-dimensional chunk action, which yields 11 chunk actions, and latent frame 0, which has no predecessor, is assigned a zero vector. This gives one action per latent frame for all 12 latent frames, with $d_a = 24$. When initializing post-training from the pretrained checkpoint, we discard the pretrained $1536 \times 32$ action embedding and allocate a new $1536 \times 24$ embedding with zero

weights and bias, so that the new action pathway is learned from scratch while all other parameters are inherited. With all parameters unfrozen, the 24-dimensional embedding is learned quickly during end-to-end post-training.

**Training objective.** Both stages use the same objective. The primary term is the rectified-flow loss of the backbone, with 1000 training timesteps and a timestep shift of $5.0$, weighted by the scheduler timestep weighting $w(t)$ and masked to the generated frames so that the given prefix is never supervised,

$$\mathcal{L}_{\text{flow}} = \frac{\sum_{b,i} m_{b,i}\, w(t_{b,i}) \left\| \mathbf{v}_\theta - \mathbf{v}^\star \right\|^2_{b,i}}{\sum_{b,i} m_{b,i}}, \qquad m_{b,i} = 1 \text{ for } i \geq k,\ 0 \text{ otherwise}, \tag{19}$$

where $\mathbf{v}_\theta$ is the predicted velocity, $\mathbf{v}^\star$ its target, and $k = 3$ the number of given prefix frames. A per-frame loss of this form is largely satisfied by a model that renders each frame plausibly while ignoring the action, since most of the latent energy sits in static anatomy. We therefore add a motion-consistency term that matches the frame-to-frame change of the prediction to that of the target,

$$\mathcal{L}_{\text{motion}} = \frac{\sum_{b,i} m_{b,i}\, w(t_{b,i}) \left\| \Delta_i \mathbf{v}_\theta - \Delta_i \mathbf{v}^\star \right\|^2}{\sum_{b,i} m_{b,i}}, \qquad \Delta_i \mathbf{v} = \mathbf{v}_i - \mathbf{v}_{i-1}, \tag{20}$$

masked to transitions ending in a generated frame, so that the handoff from the prefix to the first generated frame is included. This term measures only what changes between frames, which is precisely what the action controls. The total objective is

$$\mathcal{L} = \mathcal{L}_{\text{flow}} + \lambda\, \mathcal{L}_{\text{motion}}, \qquad \lambda = 0.1. \tag{21}$$

$\mathcal{L}_{\text{motion}}$ is computed and logged whether or not it is weighted, so the setting $\lambda = 0$ is a logging-identical control.

**Optimization.** Pretraining follows a four-stage curriculum in which each stage warm-starts the next and every stage trains the full network. A per-frame stage on single latent frames teaches speckle statistics and anatomy without any temporal burden, at an effective batch of 1536 frames; a video stage extends to whole 12-frame clips; a prefix stage adds the three-frame conditioning branch; and the final stage adds the latent-action branch. The last three stages all use an effective batch of 768 clips, so one epoch over the corpus is 201 optimizer steps. Post-training warm-starts from the final stage with the latent-action head removed. Table 9 lists the settings of both stages; they differ only in batch size and step count, which follow from the corpus sizes.

Table 9: Optimization settings. Both stages train the full network with identical optimizer, schedule and precision; the effective batch follows the corpus size.

| Setting | Pretraining | Post-training |
|---|---|---|
| Training clips | 153,892 | 262 |
| Batch (per GPU × GPUs × accum.) | $64 \times 4 \times 3$ | $8 \times 4 \times 3$ |
| Effective batch | 768 clips | 96 clips |
| Training steps | 7,236 | 18,000 |
| Prefix | $k = 3$, 9 generated | $k = 1$, 11 generated |
| Optimizer | AdamW, $\beta = (0.9, 0.999)$, weight decay $0.01$ | |
| Learning rate | $1 \times 10^{-5}$, constant | |
| Gradient clipping | 1.0, global norm | |
| Precision | bf16 mixed, FSDP with gradient checkpointing | |
| EMA decay | 0.99, started at step 100 | |
| Seed | 0 | |
| Clip geometry | 45 pixel frames → 12 latent frames | |

## B Benchmarking video VAEs for ultrasound video reconstruction

All four autoencoders reconstruct ultrasound video accurately, spanning $36.24$ to $36.62$ dB PSNR and $0.900$ to $0.922$ SSIM, a spread of $0.38$ dB and $0.022$ respectively. Autoencoders trained on

natural video therefore transfer to ultrasound without retraining, despite speckle texture and view-dependent acoustic artefacts having no counterpart in natural video. Reconstruction quality does not discriminate between the four, and they separate on cost instead. HunyuanVideo-1.5 requires 18.85 GB of peak memory against 2.22 GB for Wan2.1 and runs at half the throughput, while giving the worst LPIPS by a factor of 1.9.

We adopt the Wan2.1-T2V-1.3B autoencoder, which has the lowest peak memory and the highest throughput of the four while matching the best LPIPS at 0.033 and trailing the best PSNR by 0.12 dB. Its SSIM is the lowest of the four, by 0.022, which does not affect the downstream evaluation: generation metrics are computed against VAE-decoded ground truth rather than raw frames, so reconstruction error cancels. The margin is ample in any case. Reconstruction reaches 36.50 dB PSNR and 0.033 LPIPS, against 16.09 dB and 0.439 for causal generation in Table 1, so the autoencoder is not the bottleneck on generation quality.

Table 10: Comparison of open-source video autoencoders for ultrasound video reconstruction.

| Models | Time | Peak Memory | PSNR ↑ (dB) | SSIM ↑ | LPIPS ↓ |
|---|---|---|---|---|---|
| Wan2.1-T2V-1.3B | 0.71 clips/s | 2.22 GB | 36.50 | 0.900 | 0.033 |
| Wan2.2-TI2V-5B-Diffusers | 0.68 clips/s | 3.71 GB | 36.24 | 0.922 | 0.035 |
| HunyuanVideo-1.5 | 0.35 clips/s | 18.85 GB | 36.24 | 0.921 | 0.062 |
| LongCat-Video | 0.68 clips/s | 2.36 GB | 36.62 | 0.916 | 0.033 |

# C Additional Results

## C.1 Results on pretraining with latent actions

**Visualizations of next-frame prediction with latent actions** Figure 6 visualizes latent action model predictions on thyroid, cardiac and abdominal scans. The encoder infers a 32-dimensional latent action from a frame pair, and the decoder reconstructs the next frame from the current frame and that action alone, never seeing the next frame itself, so any predicted change must have passed through the bottleneck. The predicted frames recover the anatomy and its displacement but are smoother than the ground truth, since speckle decorrelates between frames and is not predictable from a 32-dimensional code. The two difference maps highlight the same regions in all three organs, indicating that the latent action captures transition-relevant information beyond the appearance already provided by the source frame.

**Results on video generations with latent actions.** Table 11 reports 8-second generation across the three organs. Latent actions improve every metric on every organ, by 4.74 dB PSNR, 0.114 SSIM and 0.121 LPIPS on average. The gain is largest on abdominal scans (+6.42 dB) and smallest on thyroid (+3.21 dB), while the ordering of absolute difficulty is unchanged: thyroid remains the hardest organ in both settings, reflecting its fine-scale structure and its small share of the corpus. Since the action branch is zero-initialized, the two models are identical at the start of training, so the gap measures the information the action carries. The resulting performance gap quantifies the predictive value of latent transition information beyond visual context alone. Figure 7 shows the corresponding rollouts: with latent actions, the generation tracks the ground-truth sequence, while without them it drifts into a plausible but unrelated continuation.

Table 11: Effect of latent actions on video generation across organs. We evaluate 8-second video generation conditioned on 9 initial frames (3 latent frames) on abdominal, cardiac and thyroid scans.

| | w/o latent actions | | | w/ latent actions | | |
|---|---|---|---|---|---|---|
| Organ | PSNR ↑ | SSIM ↑ | LPIPS ↓ | PSNR ↑ | SSIM ↑ | LPIPS ↓ |
| Abdomen | 16.74 | 0.618 | 0.300 | **23.16** | **0.740** | **0.180** |
| Cardiac | 17.45 | 0.660 | 0.259 | **22.02** | **0.763** | **0.156** |
| Thyroid | 14.99 | 0.378 | 0.429 | **18.20** | **0.496** | **0.290** |
| Average | 16.39 | 0.552 | 0.330 | **21.13** | **0.666** | **0.209** |

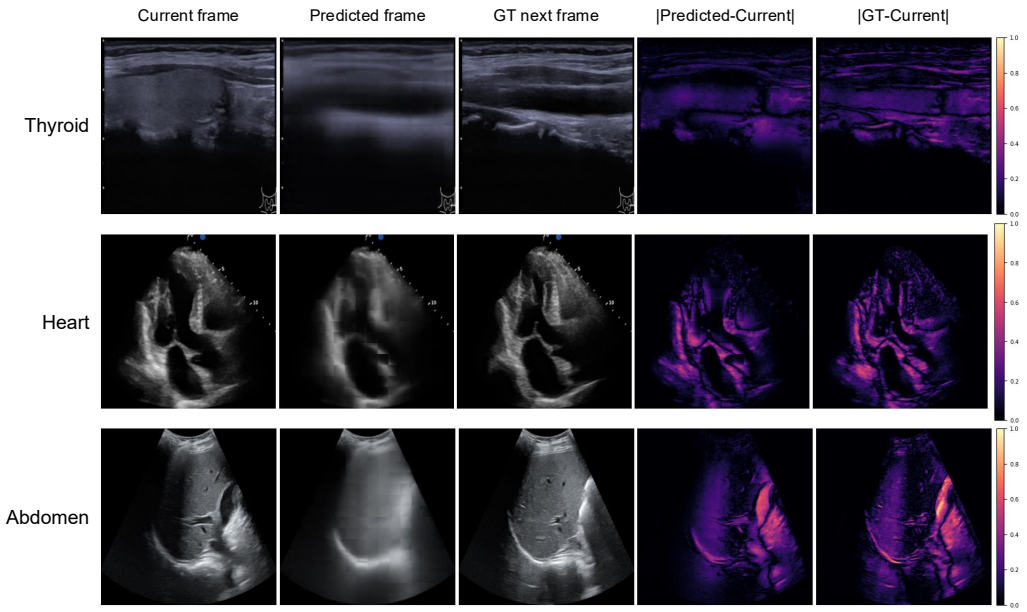


Figure 6: Latent action model predictions across organs. Rows correspond to thyroid, cardiac, and abdominal scans. Given only the current frame and the 32-dimensional latent action, the decoder predicts the next frame; the rightmost two columns show the absolute difference of the predicted and of the ground-truth next frame from the current frame.

### C.2 Results on causal inference

Figure 8 shows 8-second rollouts on three held-out scans. The causal student is trained on 3-second clips of 12 latent frames, yet at inference it extends to 33 latent frames without retraining: the generation still follows the ground-truth anatomy at $t = 8$ s, well beyond its training horizon.

## D User Study Interface

Figure 10 shows the rating interface. The left panel renders the segmented thyroid in 3D together with the probe path, the probe frame and the current imaging plane, so that raters can see where each generated frame is taken from, with a whole-gland template inset for reference. The right panel plays the generated clip with its thyroid segmentation overlaid. Raters scrub the timeline and score image quality, video consistency and probe–anatomy alignment on 5-point scales.

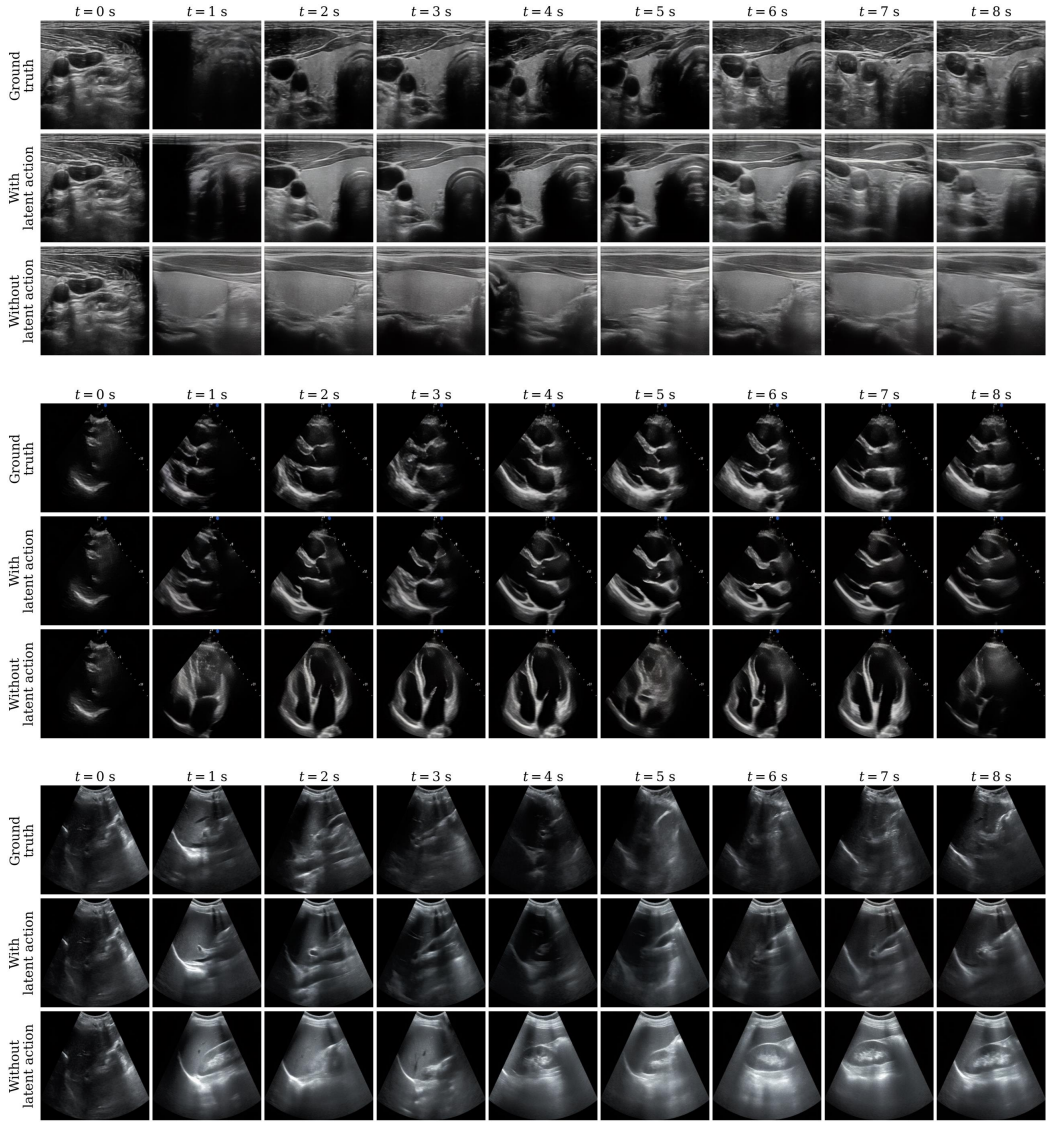


Figure 7: Generation conditioned on latent actions. Rows from top to bottom are thyroid, cardiac, and abdominal scans. The model receives the first 9 ultrasound frames and the latent action sequence, then generates the remaining ultrasound frames. Generated frames follow the ground-truth anatomy as the probe moves across all three anatomies, showing that latent-action conditioning consistently captures useful transition dynamics across all three anatomical regions.

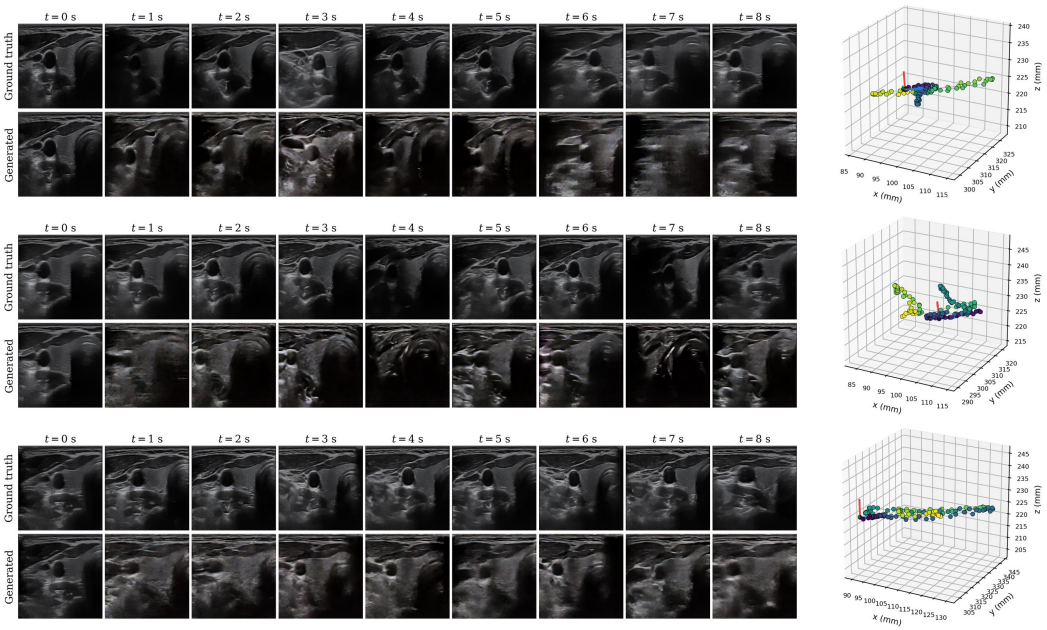


Figure 8: Eight-second rollouts from the causal model on three held-out scans. Each row is one scan: the model receives the initial frame and the measured 6-DoF pose sequence, then generates remaining frames autoregressively in four denoising steps. The right column shows the corresponding probe trajectory in the patient frame.

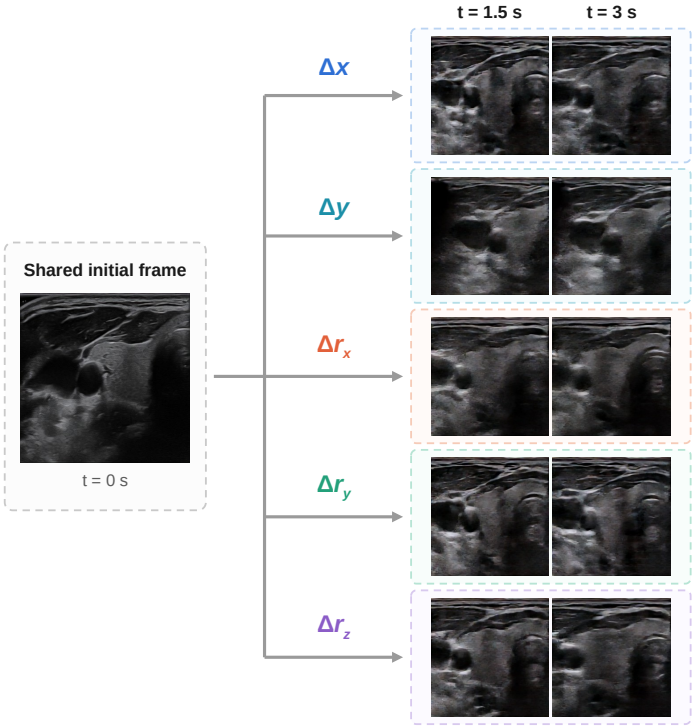


Figure 9: Generation under customized actions. Starting from the same initial frame ($t = 0\,\mathrm{s}$), SonoWorld autoregressively generates 3-second rollouts, each under a constant increment ($\Delta x$, $\Delta y$, $\Delta r_x$, $\Delta r_y$, or $\Delta r_z$) in a single degree of freedom. We set the constant increment to 1 mm in translation and 1° in rotation. The $x$, $y$, and $z$ axes correspond to the inferior–superior, left–right, and posterior–anterior directions, respectively.

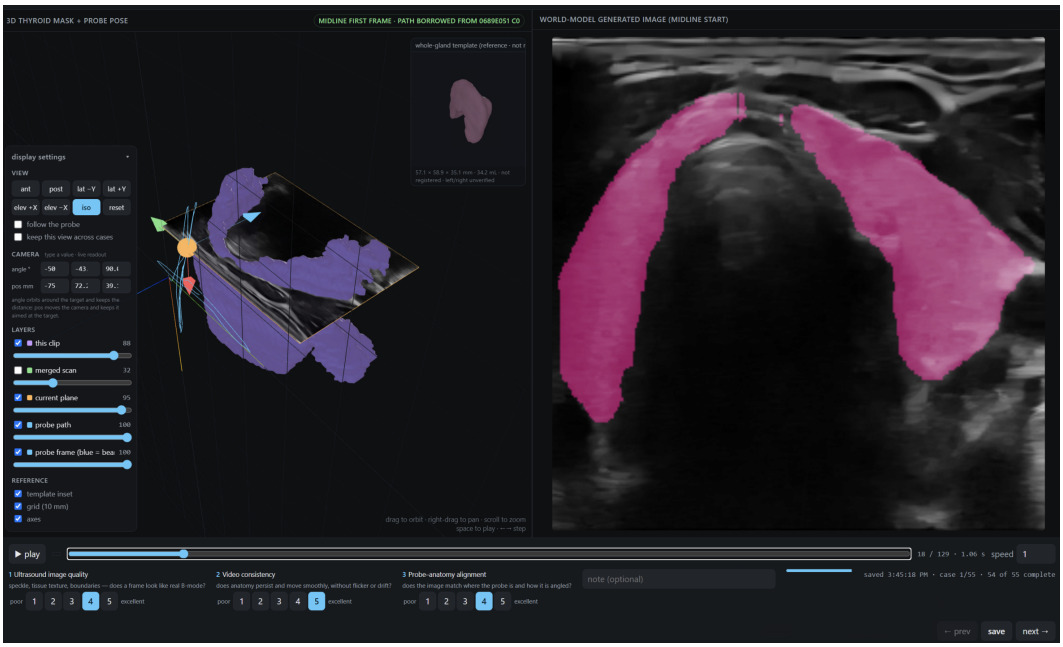


Figure 10: User study interface. Users are required to evaluate ultrasound video generated by actions according to three metrics and provide the evaluation score.